Effect of energy density on microstructure and mechanical properties of Ta−33Ti alloy prepared via laser powder bed fusion

Jia-qi ZHANG [1], Chao CHEN[1], Dan LI[1], Zhao-wen GENG[1],
Peng PAN[1], Guo-hua WANG[2], Ke-chao ZHOU[1], Jian-ling LIU[1]

1. State Key Laboratory of Powder Metallurgy, Central South University, Changsha 410083, China;

2. Hunan Huaxiang Medical Technology Co., Ltd., Ningxiang 410600, China

Abstract: The influence of laser process parameters on the densification, phase composition, microstructure, and mechanical properties of Ta−33wt.%Ti alloy prepared via laser powder bed fusion (LPBF) was investigated. The results show that fully dense and homogeneous Ta−Ti parts can be obtained from LPBF with appropriate energy input. The cellular and dendritic structures were formed due to constitutional undercooling. Transmission electron microscopy (TEM) analysis showed that the lamellar α'' phase within the cellular structures preferred to concentrate at the cellular boundaries owing to the elemental micro-segregation in the solidification front. The samples fabricated under the energy density of 166.7 J/mm^3 had a favorable ultimate tensile strength of 806 MPa and an excellent Young's modulus of 36.7 GPa.

Key words: Ta−Ti alloy; laser powder bed fusion; cellular and dendritic structures; constitutional undercooling

1 Introduction

The booming metallic biomaterials for orthopedic implants have facilitated the exploration of new biomaterials with both admirable mechanical compatibility and outstanding bio-activity [1,2]. Commercially pure titanium (Ti) and its alloys, especially Ti−6Al−4V, are considered the most suitable candidate for surgical implants due to their excellent physical and chemical properties, including high specific strength, better corrosion resistance and superior biocompatibility [3−5]. However, the significant mismatch of elastic modulus between Ti−6Al−4V alloy (110 GPa) and human bone tissues (10−30 GPa) will cause the stress shielding effect, impeding early bone-implant fixation and long-term stability [6,7]. In addition,

the release of toxic elements, such as Al and V may cause allergic reactions as well as neurological diseases [8]. Therefore, significant efforts were devoted to developing β-type titanium alloy without cytotoxic elements [9,10]. Possessing excellent physicochemical and outstanding osteogenic properties, tantalum (Ta) has shown excellent prospects in the orthopedic surgery since the introduction of the Trabecular Metal (Zimmer Biomet) [11]. However, due to its relatively high processing cost, high density, and melting point, its widespread applicability is limited [12,13].

Ta−Ti alloys, with a combination of the excellent mechanical properties of Ti and the superior biocompatibility of Ta, have emerged as an attractive bone substitute material [14]. Ta and Ti are infinitely soluble with high affinity and can form a stable continuous solid solution, giving high

strength of Ta−Ti alloy [15]. The incorporation of Ta into a Ti matrix promoted the stabilization of β (Ti,Ta) phase and the forming of Ta_2O_5 protective passive films, contributing to much lower Young's modulus and better corrosion resistance of Ta−Ti alloys [16,17]. Besides, Ta is able to promote cell adhesion and facilitates the growth of bone, enhancing the biocompatibility and osteogenesis of the Ti matrix [18]. However, owing to the remarkable difference in melting temperature (Ta: 2996 °C and Ti: 1670 °C) and density (Ta: 16.6 g/cm^3 and Ti: 4.54 g/cm^3) between Ta and Ti, the inevitable inhomogeneity and segregation of elements during the solidification hinder the broad application of Ta−Ti alloys [19]. Multiple remelting processes are often required to achieve a uniform composition by the conventional processes, which brings about a long processing period and expensive cost [20]. In addition, with considerably higher elastic moduli (69−104 GPa) compared with the elastic moduli of human bones (10−30 GPa), Ta−Ti alloys may induce bone resorption if they are implanted in the human body for a long service life [14−18].

Owing to the raw material efficiency, high designing flexibility, and digital manufacturing, additive manufacturing (AM) offers the capability to economically fabricate a wide variety of metals and customize complex geometries [21−23]. As one of the most mature technologies of AM, laser powder bed fusion (LPBF) owns the key advantages of high energy density, high accuracy, and large forming size, providing a platform for designing new alloys [24−26]. Using a high laser beam with a small spot diameter (<100 μm), LPBF can melt the refractory tantalum powder rapidly with an extremely high transient temperature exceeding 3000 °C and decrease element segregation and grain growth because of the ultrahigh cooling rate (>10^3 K/s) [27−29].

Recently, some researchers have studied the capability of producing Ti−Ta alloys by LPBF technology, proving the potential for in situ alloying and direct fabrication of functional parts [30−32]. HUANG et al [33] found that the phases showed a transformation of $\alpha\rightarrow\alpha'\rightarrow\alpha''+\alpha'\rightarrow\beta+\alpha''+\alpha'$ with the increase of Ta content. XING et al [34] and SING et al [30] fabricated Ti−50Ta alloy successfully by LPBF process using blended the Ti and Ta powders.

They reported that the process parameters had a significant effect on the density and microhardness of Ti−50Ta alloy. GAO et al [35] investigated the effect of unmelted Ta particles on the microstructures and mechanical properties of Ti−25Ta alloy. The unmelted Ta particles contributed to the toughness, ductility, and elongation of the Ti−Ta matrix but reduced the strength. ZHAO et al [36] designed a Ti−Ta gyroid scaffold with superb elastic admissible strains. The ultrafine β sub-grains and nanocrystalline α' grains gave the scaffolds a high compressive yield strength of 55.5 MPa and a low elastic modulus of 1.83 GPa. As such, through the in-situ alloying of Ti and Ta powders, LPBF-produced Ti−Ta alloys are promising materials for biomedical applications with admirable mechanical properties and bioactivity.

Overall, the previous studies focused on the densification and phase transformation of LPBF fabricated Ti−Ta alloy with the content of Ta below 50 wt.%, aiming to obtain admirable mechanical properties with high strength and low modulus. However, there have been limited attempts to additively manufacture Ti−Ta alloy at a high Ta content. Little is known about the microstructure and phase composition of LPBF fabricated Ti−Ta alloy with a high content of Ta. BRODIE et al [37] prepared the Ti−65Ta alloy with a single BCC phase alloy. However, the refractory nature of Ta may cause the vaporization of Ti as a result of the tiny gap between the melting point of Ta (2996 °C) and the boiling point of Ti (3287 °C), posing difficulties for achieving a homogenous composition under high Ta content alloy [38,39]. In addition, under the ultrahigh cooling rate of LPBF technology, non-equilibrium phases, especially the metastable α'' phase with the orthorhombic structure, will form from the β phase [40]. Therefore, systematically investigating the microstructure and phase transformation of LPBF-built Ti−Ta alloy with high Ta content is crucial to developing high-performance alloys.

In this work, a Ta−33Ti (wt.%) alloy with cellular and dendritic structures was in-situ fabricated via LPBF using mechanically mixed Ti and Ta powders. The optimum technological parameters for minimal defects were confirmed and the effect of energy density on the microstructure and mechanical properties of the prepared high Ta

content alloy were studied. In addition, the component distribution and phase composition of Ta−Ti alloy under a complicated thermal field and the ultrahigh cooling rate during the LPBF process were systematically investigated and discussed.

2 Experimental

2.1 Raw materials

An irregular hydrogenation−dehydrogenation tantalum powder (Changsha Nanfang Tantalum Niobium Ltd., China) and an ultrasonic atomized spherical titanium powder (15−53 μm, Asia New Materials Co., Ltd., Beijing, China) were used, as listed in Table 1. Tantalum powder has an oxygen content of 560×10^{-6}, while titanium powder has an oxygen content of 710×10^{-6} as determined by an oxygen and nitrogen analyzer, showing a high purity of 99.9% of raw powders. A blended mixture of 66.7 wt.% Ta and 33.3 wt.% Ti powders was conducted by a tumble mixer at a rotation speed of 60 r/min for 12 h. The micro-morphological observations of the mixed Ta−Ti powders were carried out using a field emission scanning electron microscope (FESEM, FEI Quanta 250 FEG) under the backscattering mode (BSE), and elemental analysis was carried out on this device in conjunction with energy spectroscopy (EDS). The particle size distribution of the mixed powder was measured by using a laser particle size distribution instrument (Master size R3000).

Table 1 Chemical composition of irregular Ta powder, spherical Ti powder, and mixed Ta−Ti powders (wt.%)

Powder	Ti	Ta	C	O	N
Ta	−	Bal.	0.025	0.056	0.0012
Ti	Bal.	−	0.016	0.071	0.0011
Mixed Ta−Ti	32.66	Bal.	0.018	0.068	0.0012

2.2 Sample fabrication by laser powder bed fusion

The Ta−Ti alloys of this work were in-situ fabricated by a FS33071M LPBF machine (Farsoon, Inc, China), which was equipped with an IPG YLR-500 Gaussian fiber laser owning a maximum 500 W power output, a single-mode fiber laser with an adjustable laser spot size diameter between 80

and 130 μm and a high-precision focusing $F-\theta$ lens. The samples were built on a pure titanium substrate (275 mm × 275 mm), which was sandblasted by an FS04-SBM sandblasted machine (Farsoon, Inc, China) and thoroughly cleaned with absolute ethyl alcohol before the LPBF process to avoid laser reflection and increase surface roughness. The air intake pressure during the process was set as 0.45 MPa and the sandblasted pressure was set as 0.6 MPa. The substrate was sandblasted for 5 min to ensure the first melt layer bonded to the substrate firmly. During fabrication, the build platform temperature was maintained at 100 °C, and the entire manufacturing process was conducted under a high-purity argon atmosphere in which the oxygen content was maintained below 0.1% to prevent oxidation and interstitial element contaminations such as hydrogen and nitrogen. In addition, an alternative scanning strategy in each layer rotated by 67° to its precursor was employed to reduce the thermal stress accumulated in the material during the LPBF process. After manufacturing, all samples were removed from the substrate via wire electrical discharge machining (EDM).

To investigate the influence of preparation parameters on the microstructure and densification of as-built Ta−Ti alloy, the metallographic samples (5 mm × 5 mm × 6 mm) were fabricated and their density was measured by the Archimedes' method. The key parameters in the LPBF process included laser power (P), scanning speed (v), hatch spacing (h), and layer thickness (d). To perform the process optimization for Ta−Ti alloys, the parameters of P and v were set as 200−400 W and 200−1200 mm/s, respectively, while d was controlled to 30 μm and h was fixed at 70 μm. In order to assess the energy input on the powder, the volume energy density (E) was defined by

$$E = \frac{P}{dvh} \tag{1}$$

The LPBF parameters of all Ta−Ti samples are listed in Table 2. Then the optimized parameters were utilized to fabricate the samples (20 mm × 15 mm × 10 mm) for the microstructure study and mechanical test. After the fabrication, all the samples were removed from the substrate and cut into the designed geometry using EDM.

Table 2 LPBF parameters of Ta−Ti

P/W	v/(mm·s^{-1})	h/μm	d/μm
200−400	200−1200	70	30

2.3 Metallographic characterization

For each group of parameters, three samples were tested to determine the average value of actual density. The cross-sectional area perpendicular to the build direction was processed for the metallographic analysis. The metallographic samples were embedded in epoxy resin by xQ-2B inlay machine and the cross-sections were then ground with SiC sandpaper #400, #1000, #2000, and #4000, respectively. Subsequently, they were polished by silica suspension (OPS) for 30 min and ultrasonic cleaning was conducted to remove the OPS using alcohol after polishing. The polished samples were observed using an optical microscope (OM, Leica DM2700M) to evaluate the forming quality. Image analysis was done with ImageJ software to obtain the percentage porosity.

The oxygen content of the mixed powder was investigated using an O/N/H analyzer (TCH-600). The phase identifications of LPBF Ta−33Ti sample and mixed powder were performed using X-ray diffraction (XRD, PANalytical Empyren) with Cu K$_\alpha$ (λ=1.5405 Å) radiation. The working voltage and current were 45 kV and 40 mA, respectively. XRD patterns were recorded in an angular range from 30° to 90° with a step size of 5 (°)/min.

The microstructures of as-built Ta−33Ti samples perpendicular to the build direction were observed using a scanning electron microscope (SEM, JSM−6360LV, Japan), equipped with a backscattered electron (BSE) detector, an energy dispersive spectrometer (EDS) and an electron backscatter diffraction (EBSD, Helios Nano Lab 600i) system. The composition was analyzed by EDS to verify the homogeneity of the alloy. The grain orientation, grain morphology, texture, and phase distribution of the alloy were analyzed by inverse polar pattern (IPF) generated by the EBSD using OIM software.

Transmission electron microscopy (TEM, Tecnai G2 F20) was utilized to further study the phase microstructure. To prepare the thin foil for TEM, the sample was first cut to the thickness of 0.3 mm, ground to approximately 60 μm using SiC abrasive paper, punched into 3 mm circular discs, and then ion milled to thicknesses of 40 μm. The transmission foils were electropolished for 120 s at 20 V in a 4 vol.% perchloric acid solution in ethanol at −20 °C by an automatic twin-jet polishing system.

2.4 Mechanical properties test

A uniaxial tensile test was carried out with a cupping machine (Barioe) under a strain rate of 1×10^{-3} s^{-1} at room temperature, using a video extensometer. The tensile samples (3 mm in gauge length, 1.5 mm in width, and 1 mm in thickness) were prepared by EDM and polished using up to #4000 SiC paper. For each group of parameters, no less than three individual tensile samples were tested to ensure data reproducibility. The fracture morphology was analyzed using the SEM (FEI Nova Nano230).

3 Results and discussion

3.1 Powder characteristics

The morphologies and size distribution of particles of mixed powders are shown in Fig. 1. It can be seen that the bright and irregular Ta powder particles are evenly distributed around the dark spherical Ti powder particles, as shown in Figs. 1(a, b). The particle size distribution of mixed Ta−Ti particles was D_{10}=18.4 μm, D_{50}=40.2 μm, and D_{90}=75.4 μm (Fig. 1(d)), which were especially critical in laser-based additive manufacturing. The oxygen content of the mixed Ta−33Ti powders was 680×10^{-6}, between the oxygen content of pure Ta and pure Ti powders, indicating that the powders were not over-oxidized during the mixing process.

3.2 Effect of processing parameters on densification

Figure 2 shows a density map of LPBF-processed Ta−33Ti alloy with different processing parameters, in which the red color indicates high density and blue color indicates low density. The theoretical density of the Ta−33Ti alloy was 8.79 g/cm^3 but some Ta−33Ti samples' actual densities were slightly high. The highest density reached 9.02 g/cm^3 when the P and v were 280 W, and 400 mm/s, respectively, and the energy density (E) of this processing parameter was 333.3 J/mm^3.
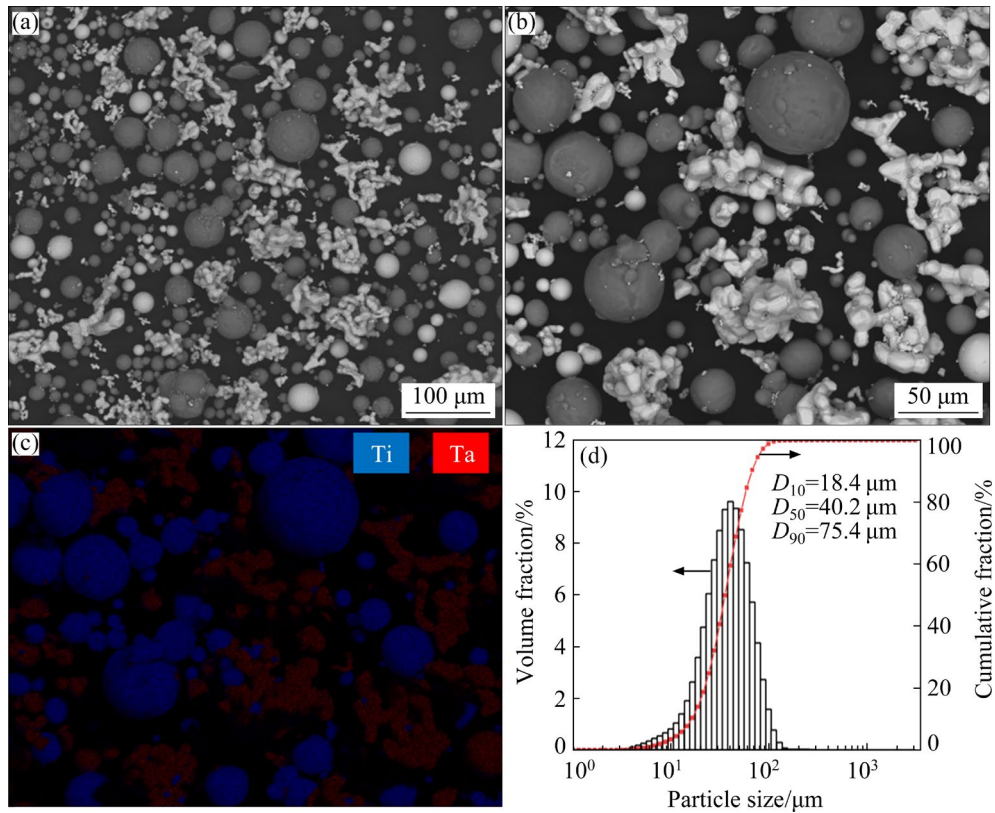
Fig. 1 BSE images (a, b) and EDS pattern (c) of Ta−Ti powders, and particle size distribution of mixed Ta−33Ti powders (d)
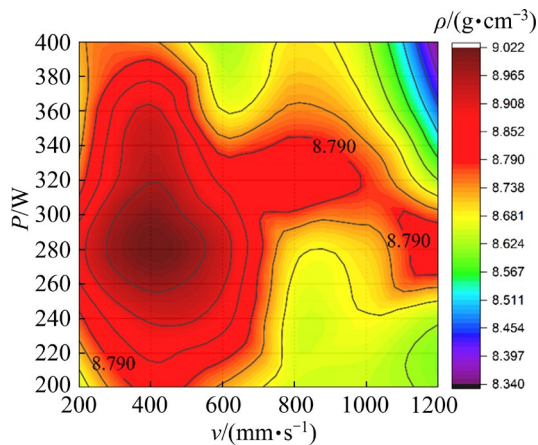

Fig. 2 Density map of as-built Ta−33Ti alloy with different laser powers and scanning speeds

As the melting point of Ta (3017 °C) and the boiling point of Ti (3287 °C) were very close, during the LPBF process, the high energy laser beam not only melted the Ta particles but also evaporated some Ti particles, leading to the reduction of Ti content in the Ta−33Ti matrix. The processing parameters of samples with high density were located in a power of 240−320 W and a speed of 200−600 mm/s, with relatively high energy

power of 190.5−761.9 J/mm^3. Under such high input energy conditions, the real mass concentration of Ti was smaller than 33 wt.%, resulting in the higher density of Ta−33Ti alloy. The actual content of Ta was confirmed and discussed by EDS in Section 3.3. To investigate the influence of energy input on microstructure and mechanical properties of LPBF-built Ta−33Ti alloy, four different processing parameters (S660−S80) were chosen for further study, as listed in Table 3.

The forming quality of LPBF-built Ta−33Ti alloy was valued by OM images with the image-based method, as shown in Fig. 3. The porosities of all samples under four parameters were 96.85%, 98.24%, 99.87%, and 95.00%, respectively. When

Table 3 LPBF parameters of Ta−33Ti sample

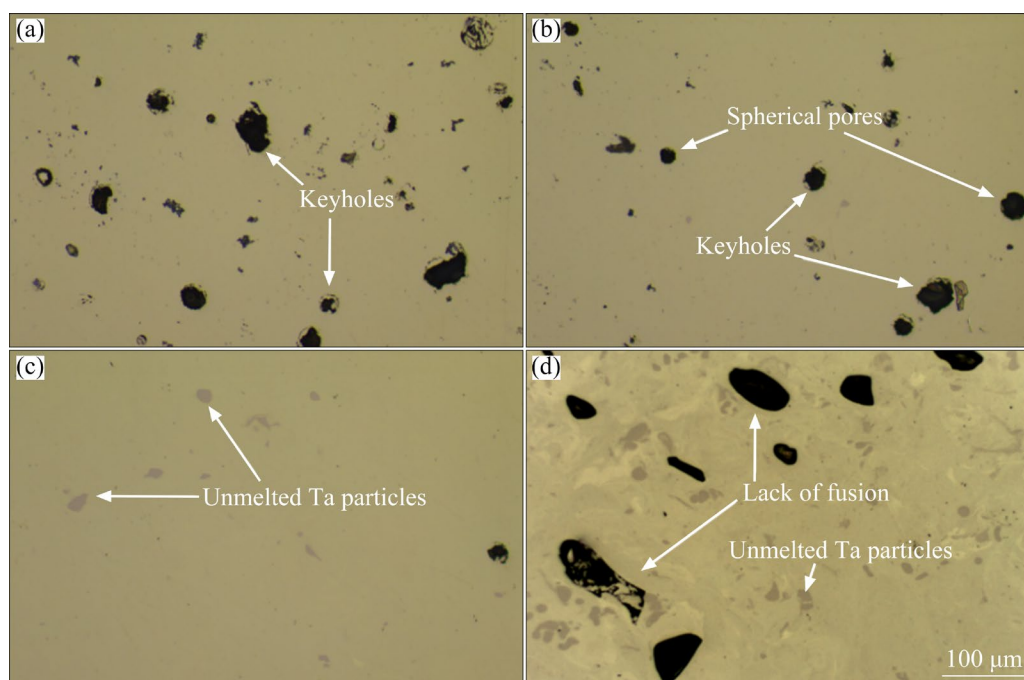| Sample	P/W	v/ (mm·s^{-1})	h/ mm	d/ mm	E/ (J·mm^{-3})
S660	280	200	0.07	0.03	666.67
S330	280	400	0.07	0.03	333.33
S160	280	800	0.07	0.03	166.67
S80	280	1600	0.07	0.03	83.33

Fig. 3 Optical micrographs of Ta−33Ti alloy at four processing parameters: (a) S660; (b) S330; (c) S160; (d) S80

P remained constant at 280 W, the energy density was inversely proportional to v. With the increase of v, an increasing trend of the amount of unmelted Ta particles was observed and the densification degree of Ta−33Ti alloy increased first and then decreased.

A large number of irregular keyholes were observed in the S660 sample, having the highest energy density ($E=666.67$ J/mm^3, $v=200$ mm/s). The keyholes were formed as a result of the occurrence of local cold zones with higher surface tension and insignificant recoil pressure [41]. When the high-energy laser scanned the powder bed, the bottom of the keyhole was heated above the evaporation point of the alloy, inducing the rise of local recoil pressure and the decline of surface tension that kept the keyhole open. However, a cold local zone formed in the upper region of the keyhole, which would close under high surface tension subsequently, leading to the formation of the keyhole. Increasing the laser power would lead to stronger and more complex fluid flow involving more vortices, much bigger melt pool volume, deeper indentation zone, and more importantly, formation of porosities. In addition, the spherical pores were generated as a result of the residual metallic titanium vapor entrapment in the solidifying molten liquid since the high cooling rate

impeded the inside vapor from escaping to the top surface in time. However, there were limited spherical holes in S660 sample because, at higher heat input, residual gas could escape to the top free surface as they had more time floating inside the larger liquid metal region. With the increase of v, the amount and size of keyholes in the S330 sample decreased and the proportion of spherical pores increased, which could be attributed to the decline of energy input. For S160 sample, there was limited pore formation as the recoil pressure was insufficient to dominate the surface tension and hence the keyhole was avoided, indicating that the energy density of S160 ($E=166.67$ J/mm^3, $v=800$ mm/s) was appropriate. Meanwhile, the medium energy input led to the appearance of tantalum particles, which could act as heat sinks that contributed to the complete fusion of the molten pool and avoided the influence of the previous layer. As shown in Fig. 3(d), the densification of the S80 sample was the worst, and a great deal of unmelted tantalum particles and lack-of-fusion defects could be seen, owing to the lowest energy density ($E=83.3$ J/mm^3, $v=1600$ mm/s). Under low energy density, the molten pool was small and shallow, which could not melt adequately the tantalum powders or the previously deposited layers, leading to the unmelted or partially melted

powder and a bad combination of the Ta−33Ti alloy.

Figures 4(a−d) show the overall morphologies of samples S660, S330, S160 and S80 under BSE mode. Consisting of OM images, many keyholes in S660, S330, and S80 samples and apparent unmelted Ta particles with irregular shapes (white regions) were observed in the Ta−Ti solid solution matrix. With the decrease in energy density, the size and the proportion of unmelted Ta increased noticeably. The variation in the proportion of unmelted Ta was made by quantitative statistics based on the statistical analysis of substantial SEM images. The unmelted Ta particles accounted for 0.02, 0.07, 1.11 and 15.63 vol.% in samples S660, S330, S160 and S80 respectively. It was obviously found that there were negligible unmelted Ta particles in the S660 and S330 samples. The high energy density contributed to the homogeneity of Ta−33Ti alloy but introduced more defects, resulting in poor densification, which would deteriorate the mechanical properties of the alloy. Few defects and unmelted Ta particles were found in the matrix of S160 sample, indicating that a proper energy density could achieve a good formation quality. In addition, it is noteworthy that the unmelted Ta particles preferred to appear at the boundaries of the melting pool. The rapid solidification impeded the diffusion of Ta, leaving some regions solidified before Ta was completely diffused and homogenized the region. Therefore, most of the Ta-poor areas, especially the melting pool boundaries, tend to show unmelted or incompletely diffused Ta particles. With the lowest energy density, the percentage and size of unmelted Ta particles increased significantly and a large number of pores appeared in S80 samples. Considering the terrible formation and compositional heterogeneity of the S80 sample, it was not chosen for further investigation in this study. Consequently, it is worth mentioning that tuning the energy density is very effective for reducing the unmelted Ta particles and achieving homogeneity of Ta−Ti alloys.

3.3 Microstructure of LPBF-built Ta−Ti alloy

The uniformity of element distribution and quantification of Ta was investigated by EDS mapping for the three Ta−33Ti samples (S660, S330, and S160), as shown in Figs. 5(a−c). The Ta
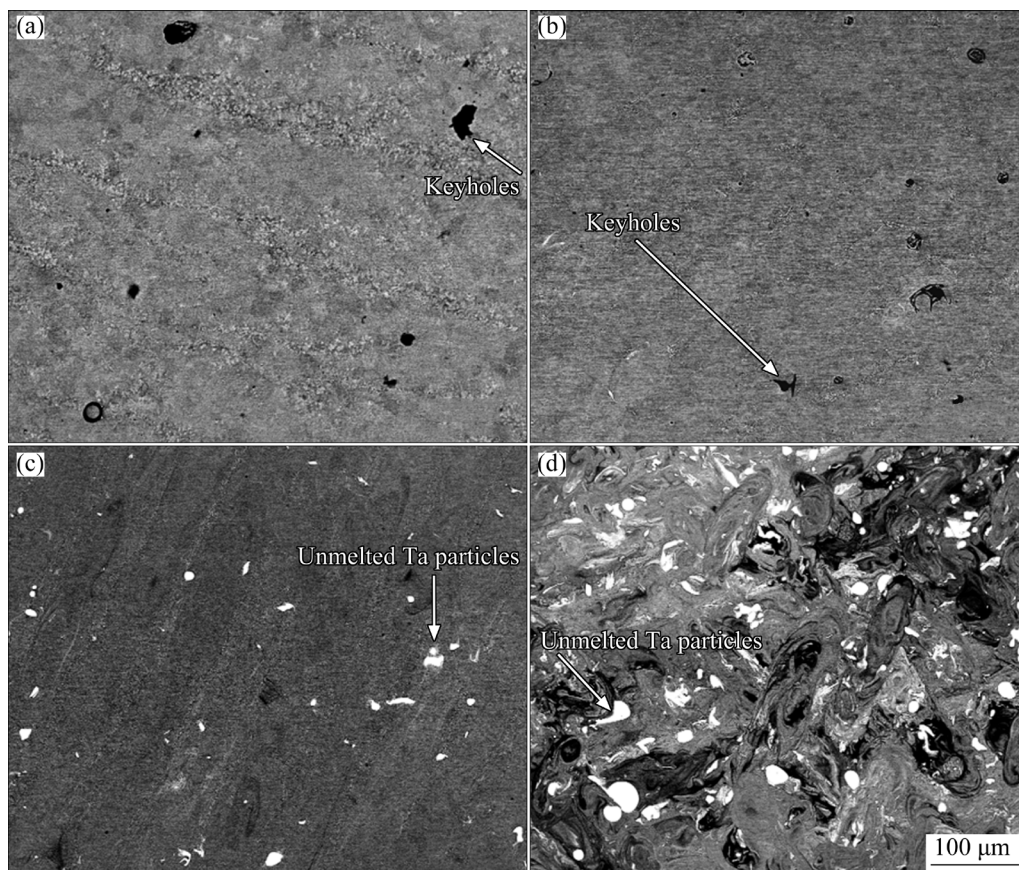

Fig. 4 SEM images of Ta−33Ti alloy obtained at four processing parameters: (a) S660; (b) S330; (c) S160; (d) S80

compositions of three samples under different energy densities were 70.68 wt.%, 66.18 wt.%, and 64.24 wt.%, respectively.

At the lowest scanning speed, the dwelling time on the melting pool of the laser beam was long, resulting in a high temperature of the melting pool, which not only melted Ta fully but also caused the evaporation of Ti. Therefore, the S660 sample had the highest Ta content among the three samples and its true density was larger than the theoretical density. The input energy densities of S330 and S160 were lower than that of S660, leading to a lower Ta content in the matrix. With a moderate energy density, Ta contents in S330 and S160 were similar to the designed composition.

The obvious cellular and dendritic structures were seen in the LPBF-built Ta−33Ti alloy at high magnification (Fig. 6). The dendrites with a width of 1−3 μm appeared along the melt track and grew towards the center of the melting pool, as shown in Figs. 6(b, e, h). Within the melting pool, the irregular cellular structure with a diameter of 3−15 μm was observed in Figs. 6(c, f, i). It was worth noting that there was obvious bright contrast within the dendrites at high magnification in the insert image of Fig. 6(h), which means that apparent

elemental micro-segregation occurred during the LPBF process. The observed microstructure is consistent with a similar LPBF-fabricated Ti−Ta study [34].

The formation of cellular and dendritic structures can be related to the constitutional undercooling during rapid cooling cycles in the LPBF process as

$$\frac{G}{R} < \frac{T_{eq}}{D_{L}} \tag{2}$$

where R is the solid growth rate, G is the temperature gradient ahead of the solidification front, T_{eq} is the equilibrium solidification range of the alloy, and D_{L} is the solute diffusivity in the liquid [33].

During the LPBF process, the rapid solidification leads to limited Ta diffusion and the content of solid Ta is higher at the liquid−solid interface, which causes Ti to be rejected by the solid into the solidification front in the liquid and Ti needed to be transported away from the interface. Then, a compositional gradient ahead of the solidification front occurs, which translates to the variation in the liquidus temperature. The formation of cellular structure within the melting pool in
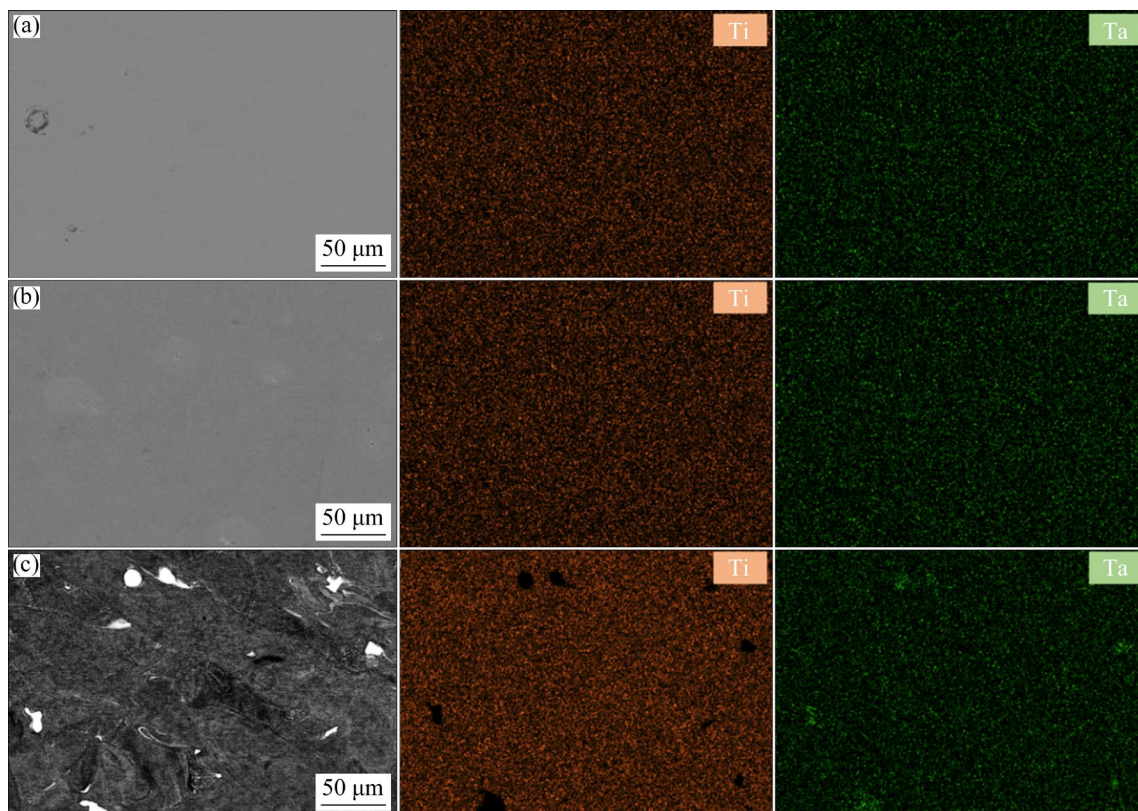

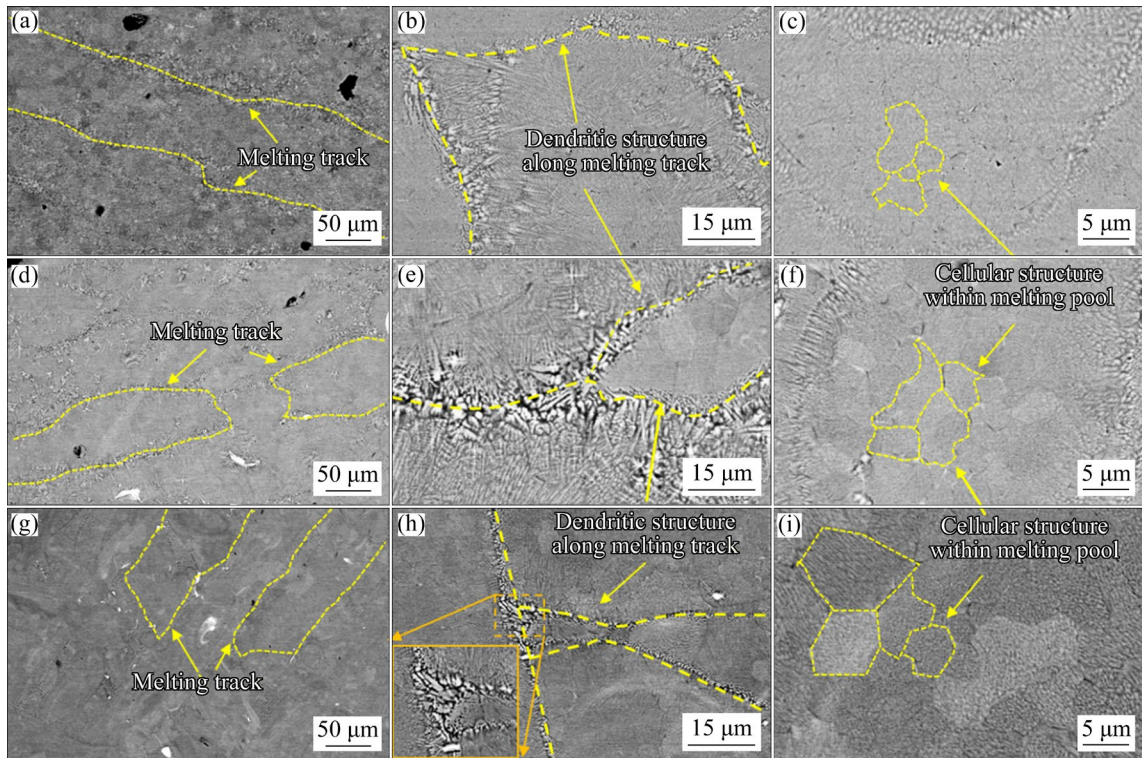**Fig. 5** EDS surface scanning results of S660 (a), S330 (b) and S160 (c) samples

Fig. 6 Backscattered electron (BSE) images of S660 (a−c), S330 (d−f) and S160 (g−i) samples

LPBF-built Ta−33Ti alloy can be attributed to the condition that the G/R ratio is only slightly smaller than the T_{eq}/D_L ratio. When the G/R ratio is much smaller than the T_{eq}/D_L ratio, especially at the boundaries of the melting pool, the cellular structure turns into a columnar dendritic [42]. In addition, the width of the dendritic in Ta−33Ti alloy can be closely associated with the content of the compositional gradient. With higher input energy density, higher temperature gradient, and higher solidification rate, the S660 and S330 samples had a larger width of dendritic compared with the S160 sample.

3.4 Phase identification of LPBF-built Ta−Ti alloy

The phases of the LPBF-built Ta−33Ti samples with different energy densities were detected by XRD, as shown in Fig. 7. The α and β phases were identified in the mixed raw powders by XRD according to the standard PDF card. However, the pattern of all LPBF-fabricated samples only identified the β phase, which means that in a high mass fraction Ta, Ti and Ta tended to form a solid solution. The α'' phase was not detected, which might be attributed to the tiny content and limitation of instrument precision.
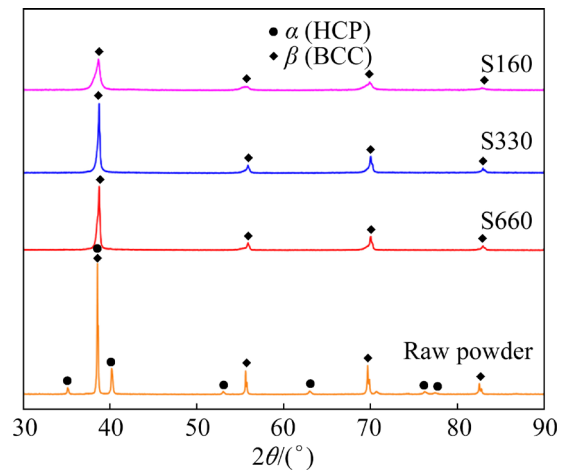

Fig. 7 XRD patterns of Ta−33Ti alloy with different energy densities

Figure 8 elucidates the inverse pole figure (IPF) images of the grain orientation of S660, S330 and S160 samples. Each grain was color-coded according to reference crystal orientation. Both the three samples were dominated by the β phase with random grain orientation. The grain sizes of S660, S330 and S160 samples were 5.01, 4.79 and 6.20 μm, respectively, as shown in Figs. 8(b, d, f). The microstructure morphology of the three samples was similar, as shown in IPF maps. Vertical
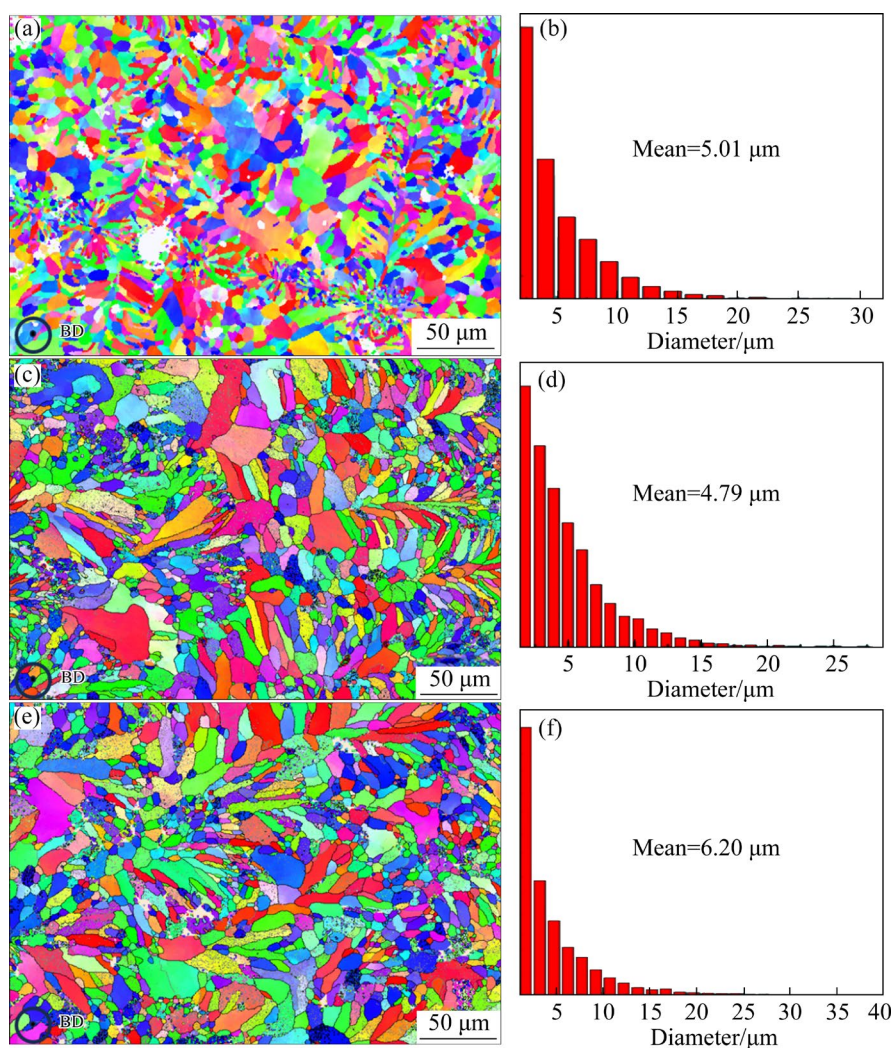
Fig. 8 IPF maps of EBSD (a, c, e) and corresponding grain size distribution (b, d, f): (a, b) S660; (c, d) S330; (e, f) S160

to the building direction, the melting tracks could be distinguished apparently, where the equiaxed β grain preferred to occur. Depending on the constitutional undercooling, the ratio of G/R along the melting track was lower than the region away from the melting track, causing the equiaxed grain to form along the tracks while the columnar grain tended to form between the tracks. The grain size of the three samples was very similar, which means that the energy density had little influence on the grain size of the Ta−33Ti alloy. The cellular and dendritic structures found in SEM images cannot be interpreted as a grain because the adjacent cells have almost the same crystallographic orientation as shown in Fig. 8. It should be noted that several black-colored unindexed areas can be seen in the IPF maps because of the compositional segregation that causes phase differences as well as continuous changes in lattice constant.

As a beta stabilizer element, Ta suppresses the transformation of β to α' phase by dropping the martensitic start temperature. The stability of the BCC structure depends on the amount of alloying elements according to molybdenum equivalency [43]. With a high content of Ta, the β phase preferred to be retained in Ta−33Ti alloy. However, owing to the constitutional undercooling during the LPBF process, the compositional segregation of Ti at the boundaries of the melting pool might lead to the formation of α'' martensite [34]. To investigate the phase composition of Ta−33Ti alloy, the TEM observation was performed on S660, S330 and S160 samples.

As shown in the bright-field images and SAED images in Fig. 9, the S660 sample was composed of mainly β phase, and a rare α'' phase was found. There were few α'' phases found in the S330 sample but lots of lamellar α'' martensite distributed in

the β matrix of the S160 sample. The phase structure of Ti−Ta alloy was dependent on their composition [44]. According to Fig. 5, owing to the varying degrees of evaporation of Ti, the Ta compositions of three samples (S660, S330 and S160) were 70.68 wt.%, 66.18 wt.% and 64.24 wt.%, respectively, leading to a difference of their phase composition.

A more detailed TEM observation was performed on the cellular structure in the S160 sample to study the formation of lamellar α'' martensite. As shown in a dark-field image in Fig. 10(a), the cellular structure showed a morphology consisting of a cellular boundary (dark region) and a bright region within the cells. The corresponding selected area electron diffraction
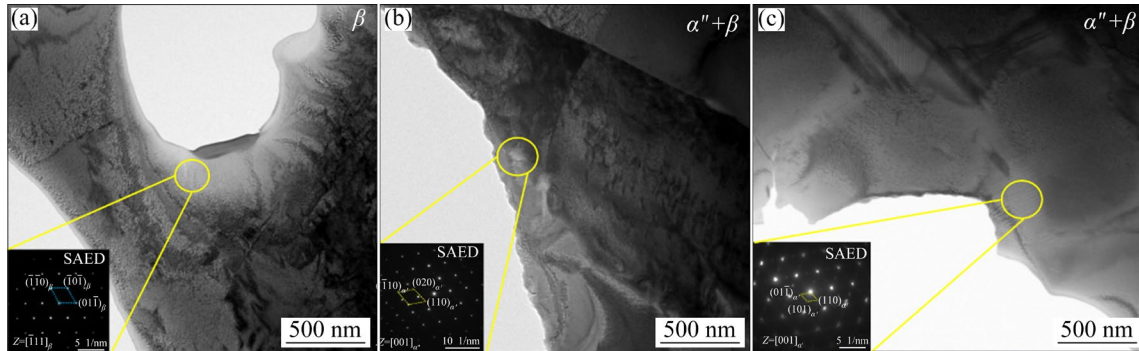

Fig. 9 Bright-field images and SAED images of S660 (a), S330 (b) and S160 (c) samples
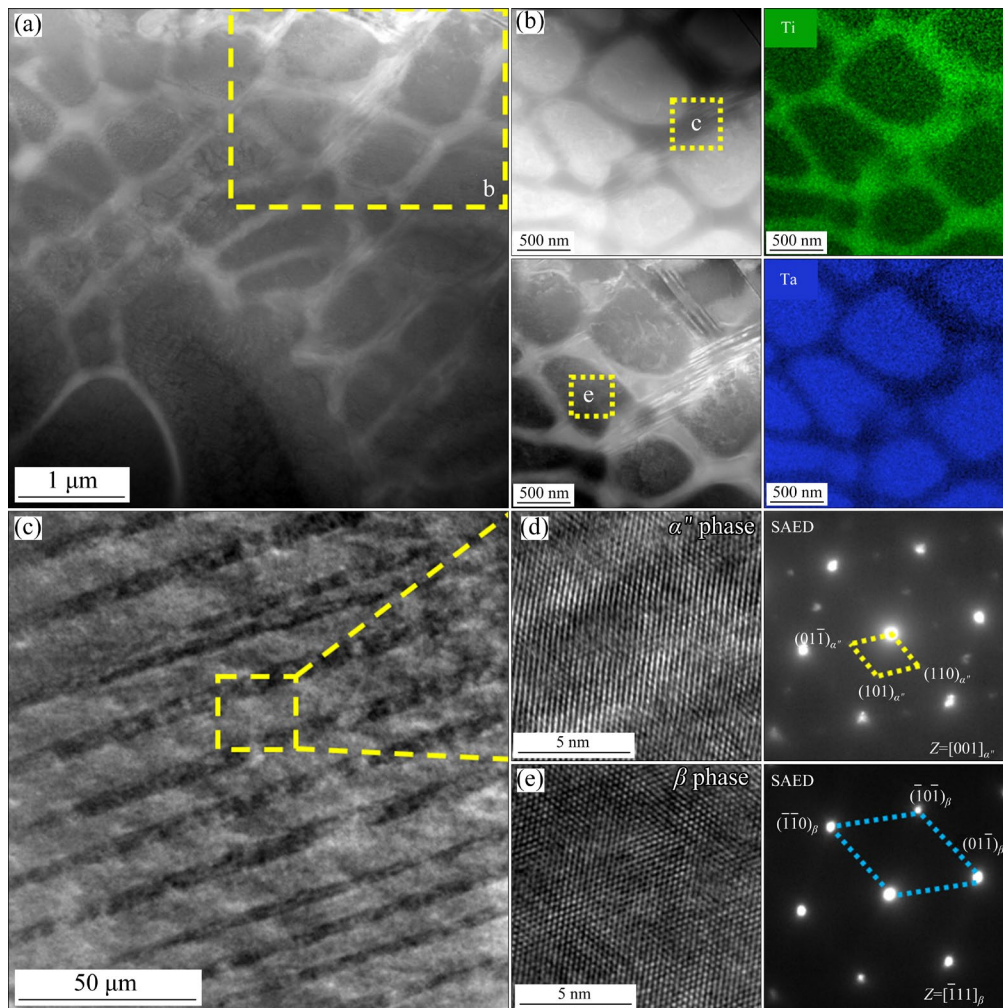

Fig. 10 TEM images of S160 sample for identifying phases: (a, c) Dark-field images; (b) Bright-field and dark-field image and corresponding elemental distribution; (d, e) HRTEM images and corresponding SAED images

(SAED) images in Figs. 10(d, e) indicated the α'' and β phases with their high-resolution transmission electron microscopy (HRTEM) images. Figure 10(c) depicts a dark-field image, exhibiting the lamellar α'' martensite with the size of dozens of nanometers orderly distributed in the β matrix. The EDS mapping results for the dark field image in Fig. 10(b) suggest that the content of Ti is higher in the α'' phase, which means that an elemental micro-segregation occurs in the cellular boundary within the cellular structure.

Similar to the previous study of the Ti−50Ta alloy [34], the LPBF-built Ta−33Ti alloy had a phase composition of α'' and β phases and the metastable α'' phase was distributed at the cellular boundaries within the cellular structure. As discussed earlier, with a high Ta content of Ta−33Ti alloy, the phase transition of $\beta \rightarrow \alpha'$ is suppressed completely and the β phase is retained. However, owing to the constitutional supercooling during the process of rapid cooling, the content of Ti is higher in the cellular boundary within the cellular structure, leading to the $\beta \rightarrow \alpha''$ transition.

3.5 Mechanical properties of LPBF-built Ta−Ti alloy

The quasi-static uniaxial tensile tests were performed on the LPBF-built Ta−33Ti samples at different energy densities. The engineering stress−strain curves and mechanical properties are displayed in Fig. 11 and Table 4, respectively. As shown in Fig. 11, the variation in energy density had a significant effect on ultimate tensile strength and elongation. With the decrease in energy density, the ultimate tensile strength (UTS) decreased and
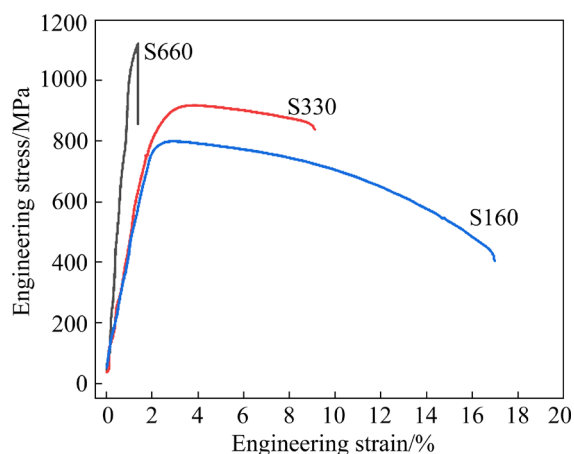

Fig. 11 Engineering stress−engineering strain curves of Ta−33Ti sample at various energy densities

Table 4 Tensile properties of Ti−Ta, pure Ta and TC4 fabricated by LPBF

Sample	Ultimate tensile strength/MPa	Elongation/%	Young's modulus/GPa
S660	1014.71±82.99	1.33±0.05	99.31±4.55
S330	884.11±34.08	10.87±1.56	42.57±1.32
S160	806.09±9.38	15.66±1.27	36.70±2.11
Ta [33]	632±11	26.0±2.6	187±4
TC4 [33]	1204±10	9.1±0.3	148±1
Ti−25Ta [33]	771±30	31.0±1.0	65±2
Ti−50Ta [45]	924.64±9.06	11.72±1.13	75.77±4.04

the elongation after fracture was increased. It is worth noting that S330 and S160 samples exhibit not only high strength but also low modulus that is close to the elastic modulus of human bones, which is very favorable for bone healing and remodeling.

The high mechanical strength of LPBF-produced Ti−Ta alloy can be attributed to a synthetic combination of solid-solution strengthening, grain refining strengthening, and dislocation strengthening. The S660 sample, with the highest input energy, had no plastic stage and the fracture occurred almost at the elastic stage because of the high porosity. The initial internal defects had a serious impact on the mechanical properties. The outstanding UTS of S660 sample (1015 MPa) might be attributed to the massive solid-solution strengthening as a result of high Ta content. With a lower input energy density, there were few defects in S330 and S160 samples, leading to a significant improvement in ductility. Dominated by β phase and twin-type lamellar α'' martensite, both S330 and S160 samples showed an increase in UTS compared with the conventionally fabricated Ti−Ta alloys (560 MPa [46]) and a great improvement in elongation compared with the S660. The twin interfaces between α'' martensites can impede dislocation motion during plastic deformation, improving the strain-hardening rate and stabilizing the plastic flow behavior. This phenomenon was also called twining-induced plasticity (TWIP), which was frequently observed in other titanium alloys [47]. The content of α'' phase in the S160 sample was higher than that of the S330 sample, resulting in a greatly increase of elongation (15.66%) in S160 than S330 (10.87%). Besides, GAO et al [35] found that the unmelted Ta particles were significantly elongated along the tensile
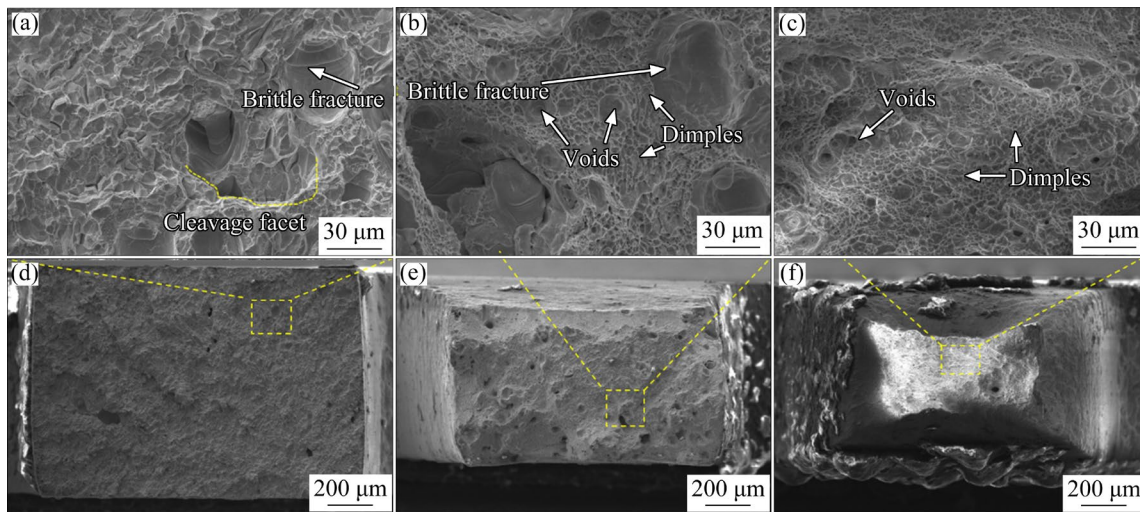
Fig. 12 Morphologies of cross-sectional fracture with different magnifications in samples S660 (a, d), S330 (b, e), and S160 (c, f)

direction, which undertook a large amount of deformation. Therefore, the unmelted Ta particles contributed to the ductility of S160 and S330 as well. The outstanding modulus of S330 and S160 might be attributed to the ultrafine cellular β sub-grains in the matrix, which reduced the elastic modulus greatly [31].

The tensile fracture morphologies of Ta−33Ti with various input energy densities are presented in Fig. 12. There are significant differences in fracture type of the three samples. There were apparent cleavage facets and no shrinkage at the fracture of S660 in Figs. 12(a, d), showing the characteristics of brittle fracture, which can be related to the poor densification of S660. The fractographies of S330 display shallow ductile dimples and cleavage facets (Figs. 12(b, e)), which means that S330 exhibits a mixture of ductile and brittle fractures. However, as shown in Figs. 12(c, f), a large number of deep dimples, voids, and obvious shrinkage can be seen in S160, indicating the characteristics of ductile fracture. The plasticity was directly related to the defects, and the elongation correspondingly appeared to increase with the decrease in energy density.

4 Conclusions

(1) Laser power and scanning speed have a significant effect on the density and porosity of LPBF-prepared Ta−33Ti alloy. Under high energy density, Ta particles can be molten sufficiently but

lead to quite a few pores and defects. Owing to the evaporation, the Ti content in the Ta−Ti matrix decreases with the increase of energy. The fully dense Ta−33Ti alloy (>99.9%) with few unmelted Ta particles was obtained with an energy of 166.67 J/mm^3.

(2) The heat accumulation and supercooling degree of the LPBF process had a great influence on the microstructure of Ta−33Ti alloy, which was dominated by cellular and dendritic structures. With the decrease of energy density, the evaporation of Ti decreases, contributing to the $\beta \rightarrow \alpha''$ transition. Owning to the segregation of Ti in the solidification front, orthorhombic α'' martensite preferred to concentrate on the cellular boundaries.

(3) The mechanical property of LPBF-prepared Ta−33Ti alloy was dependent on the energy density. With the increase of input energy density, the UTS of Ta−33Ti alloy increased while the elongation decreased. The sample prepared with 166.7 J/mm^3 achieved a favorable strength of 806 MPa and an excellent modulus of 36.7 GPa simultaneously.

CRediT authorship contribution statement

Jia-qi ZHANG: Conceptualization, Data curation, Investigation, Writing – Original draft; **Chao CHEN:** Methodology, Formal analysis, Writing – Review & editing, Funding acquisition; **Dan LI:** Methodology, Data curation; **Zhao-wen GENG:** Validation, Visualization; **Peng PAN：** Conceptualization, Formal analysis; **Guo-hua WANG:** Methodology, Resources; **Ke-chao ZHOU:** Investigation, Supervision; **Jian-ling**

LIU: Formal analysis, Supervision.

Declaration of competing interest

Acknowledgments

References

[1]   ZADPOOR A A. Meta-biomaterials [J]. Biomaterials Science, 2019, 8(1): 18−38.

[2]   LEI Peng-fei, QIAN Hu, ZHANG Tao-mei, LEI Ting, HU Yi-he, CHEN Chao, ZHOU Ke-chao. Porous tantalum structure integrated on Ti6Al4V base by laser powder bed fusion for enhanced bony-ingrowth implants: In vitro and in vivo validation [J]. Bioactive Materials, 2022, 7: 3−13.

[3]   ZHANG Tao-mei, CHEN Chao, DONG Jing, WU Yi-you, QIAN Hu, LEI Ting, LEI Peng-fei, ZHOU Ke-chao. Microstructure and biocompatibility of porous-Ta/Ti−6Al−4V component produced by laser powder bed fusion for orthopedic implants [J]. Materials Characterization, 2021, 182: 111554.

[4]   CVIJOVIĆ-ALAGIĆ I, LAKETIĆ S, MOMČILOVIĆ M, CIGANOVIĆ J, VELJOVIĆ Đ, BAJAT J, KOJIĆ V, RAKIN M. Laser processing effects on Ti−45Nb alloy surface, corrosive and biocompatible properties [J]. Transactions of Nonferrous Metals Society of China, 2024, 34(8): 2533−2551.

[5]   LIU Zheng, ZHANG Lian-min, REN De-chun, MA Ai-li, JI Hai-bin, ZHENG Yu-gui. Corrosion behavior of Ti−6Al−4V alloy fabricated by selective laser melting in simulated spent fuel reprocessing environment [J]. Transactions of Nonferrous Metals Society of China, 2024, 34(7): 2167−2180.

[6]   RIDZWAN M I Z, SHUIB S, HASSAN A Y, SHOKRI A A, IBRAHIM M N M. Problem of stress shielding and improvement to the hip implant designs: A Review [J]. Journal of Medical Sciences, 2007, 7(3): 460−467.

[7]   SHAH F A, THOMSEN P, PALMQUIST A. Osseointegration and current interpretations of the bone-implant interface [J]. Acta Biomaterialia, 2019, 84: 1−15.

[8]   ZHANG Lai-chang, CHEN Liang-yu. A review on biomedical titanium alloys: Recent progress and prospect [J]. Advanced Engineering Materials, 2019, 21(4): 1801215.

[9]   QI Peng, LI Bo-long, WANG Tong-bo, ZHOU Lian, NIE Zuo-ren. Microstructure and properties of a novel ternary Ti−6Zr−xFe alloy for biomedical applications [J]. Journal of

Alloys and Compounds, 2021, 854: 157119.

[10] WANG Xin-nan, HAN Ming, ZHANG Fu-rong, ZHAO Guang-ming, ZHU Zhi-shou. A new rhombohedral phase and its 48 variants in β titanium alloy [J]. Transactions of Nonferrous Metals Society of China, 2024, 34(9): 2849−2863.

[11] RUSSELL S P, O'NEILL C J, FAHEY E J, GUERIN S, GUL R, HARTY J A. Trabecular metal augments for severe acetabular defects in revision hip arthroplasty: A long-term follow-up [J]. The Journal of Arthroplasty, 2021, 36(5): 1740−1745.

[12] WU Yi-ping, WANG Guo-hua, ZHANG Tao-mei, LI Dan, ZHANG Jia-qi, LIU Shi-jie, CHEN Chao, ZHOU Ke-chao. Effect of CH_4 on plasma spheroidization of tantalum powder [J]. Powder Technology, 2024, 437: 119523.

[13] WEI Xue, XIA Long-gong, LIU Zhi-hong, ZHANG Le-ru, LI Qi-hou. A review of tantalum resources and its production [J]. Transactions of Nonferrous Metals Society of China, 2023, 33(10): 3132−3156.

[14] BRODIE E G, ROBINSON K J, SIGSTON E, MOLOTNIKOV A, FRITH J E. Osteogenic potential of additively manufactured TiTa alloys [J]. ACS Applied Bio Materials, 2021, 4(1): 1003−1014.

[15] XU Sheng-hang, LIU Yong, YANG Chao, ZHAO Heng-lv, LIN Bin, LI Jian-bo, SONG Min. Compositionally gradient Ti−Ta metal-metal composite with ultra-high strength [J]. Materials Science and Engineering A, 2018, 712: 386−393.

[16] LIU Yong, LI Kai-yang, WU Hong, SONG Min, WANG Wen, LI Nian-feng, TANG Hui-ping. Synthesis of Ti−Ta alloys with dual structure by incomplete diffusion between elemental powders [J]. Journal of the Mechanical Behavior of Biomedical Materials, 2015, 51: 302−312.

[17] LIU Chang-chang, LI Yang-huan-zi, GU Ji, SONG Min. Phase transformation in titanium alloys: A review [J]. Transactions of Nonferrous Metals Society of China, 2024, 34(10): 3093−3117.

[18] ZHANG Yi-neng, YANG Hai-lin, JUAIM A N, CHEN Xiao-na, LU Chang, ZOU Ling, WANG Yin-zhou, ZHOU Xiong-wen. Biocompatibility and osteogenic activity of Zr−30Ta and Zr−25Ta−5Ti sintered alloys for dental and orthopedic implants [J]. Transactions of Nonferrous Metals Society of China, 2023, 33(3): 851−864.

[19] DERCZ G, MATUŁA I, ZUBKO M, KAZEK-KĘSIK A, MASZYBROCKA J, SIMKA W, DERCZ J, ŚWIEC P, JENDRZEJEWSKA I. Synthesis of porous Ti−50Ta alloy by powder metallurgy [J]. Materials Characterization, 2018, 142: 124−136.

[20] MORITA A, FUKUI H, TADANO H, HAYASHI S, HASEGAWA J, NIINOMI M. Alloying titanium and tantalum by cold crucible levitation melting (CCLM) furnace [J]. Materials Science and Engineering A, 2000, 280(1): 208−213.

[21] GENG Zhao-wen, CHEN Chao, SONG Miao, LUO Jin-ru, CHEN Jia-xuan, LI Rui-di, ZHOU Ke-chao. High strength Al0.7CoCrFeNi2.4 hypereutectic high entropy alloy fabricated by laser powder bed fusion via triple-nanoprecipitation [J]. Journal of Materials Science & Technology, 2024, 187: 141−155.

[22] LI Dan, WU Yi-you, GENG Zhao-wen, ZHANG Jia-qi, CHEN Chao, LIU Xiao-chun, LIU Yang, ZHOU Ke-chao. High strength Al−Mg−Sc−Zr alloy with heterogeneous grain structure and intragranular precipitation produced by laser powder bed fusion [J]. Journal of Alloys and Compounds, 2023, 939: 168722.

[23] TAO Hui, LI Hui-zhong, LI Jia-hui, WANG Li, HE Wei-wei, TAN Xiao-fen, ZHOU Rui, LIANG Xiao-peng. Microstructural evolution and dynamic recrystallization mechanisms of additively manufactured TiAl alloy with heterogeneous microstructure during hot compression [J]. Transactions of Nonferrous Metals Society of China, 2024, 34(10): 3208−3220.

[24] GENG Zhao-wen, CHEN Chao, LI Rui-di, LUO Jin-ru, ZHOU Ke-chao. Composition inhomogeneity reduces cracking susceptibility in additively manufactured AlCoCr-FeNi2.1 eutectic high-entropy alloy produced by laser powder bed fusion [J]. Additive Manufacturing, 2022, 56: 102941.

[25] DING Rou, DENG Jun-wang, LIU Xiao-chun, WU Yi-you, GENG Zhao-wen, LI Dan, ZHANG Tao-mei, CHEN Chao, ZHOU Ke-chao. Enhanced mechanical properties and thermal stability in additively manufactured Al−Ni alloy by Sc addition [J]. Journal of Alloys and Compounds, 2023, 934: 167894.

[26] GENG Yao-xiang, ZAI Chun-feng, YU Jiang, TANG Hao, LÜ Hong-wei, ZHANG Zhi-jie. Strength and plasticity improvement induced by strong grain refinement after Zr alloying in selective laser-melted AlSiMg1.4 alloy [J]. Transactions of Nonferrous Metals Society of China, 2024, 34(9): 2733−2742.

[27] YANG Zi-wei, CHEN Chao, LI Dan, WU Yi-you, GENG Zhao-wen, KONAKOV V, ZHOU Ke-chao. An additively manufactured heat-resistant Al−Ce−Sc−Zr alloy: Microstructure, mechanical properties and thermal stability [J]. Materials Science and Engineering A, 2023, 872: 144965.

[28] LIU Min, ZHANG Jia-qi, CHEN Chao, GENG Zhao-wen, WU Yi-you, LI Dan, ZHANG Tao-mei, GUO Yu. Additive manufacturing of pure niobium by laser powder bed fusion: Microstructure, mechanical behavior and oxygen assisted embrittlement [J]. Materials Science and Engineering A, 2023, 866: 144691.

[29] XU Rui-feng, GENG Zhao-wen, WU Yi-you, CHEN Chao, NI Mang, LI Dan, ZHANG Tao-mei, HUANG Hong-tao, LIU Feng, LI Rui-di, ZHOU Ke-chao. Microstructure and mechanical properties of in-situ oxide-dispersion-strengthened NiCrFeY alloy produced by laser powder bed fusion [J]. Advanced Powder Materials, 2022, 1(4): 100056.

[30] SING S L, WIRIA F E, YEONG W Y. Selective laser melting of titanium alloy with 50 wt% tantalum: Effect of laser process parameters on part quality [J]. International Journal of Refractory Metals and Hard Materials, 2018, 77: 120−127.

[31] ZHAO Dan-lei, HAN Chang-jun, LI Yan, LI Jing-jing, ZHOU Kun, WEI Qing-song, LIU Jie, SHI Yu-sheng. Improvement on mechanical properties and corrosion resistance of titanium-tantalum alloys in-situ fabricated via selective laser melting [J]. Journal of Alloys and Compounds,

2019, 804: 288−298.

[32] BRODIE E G, RICHTER J, WEGENER T, NIENDORF T, MOLOTNIKOV A. Low-cycle fatigue performance of remelted laser powder bed fusion (L-PBF) biomedical Ti25Ta [J]. Materials Science and Engineering A, 2020, 798: 140228.

[33] HUANG Sheng, SING S L, de LOOZE G, WILSON R, YEONG W Y. Laser powder bed fusion of titanium−tantalum alloys: Compositions and designs for biomedical applications [J]. Journal of the Mechanical Behavior of Biomedical Materials, 2020, 108: 103775.

[34] XING Lei-lei, ZHAO Cong-cong, CHEN Hao, SHEN Zhi-jian, LIU Wei. Microstructure of a Ti−50wt.%Ta alloy produced via laser powder bed fusion [J]. Acta Metallurgica Sinica (English Letters), 2020, 33(7): 981−990.

[35] GAO Mu, HE Ding-yong, CUI Li, MA Li-xia, TAN Zhen, ZHOU Zheng, GUO Xing-ye. Investigation on the micro-structure and mechanical properties of the Ti−Ta alloy with unmelted Ta particles by laser powder bed fusion [J]. Materials, 2023, 16(6): 2208.

[36] ZHAO Dan-lei, LIANG Hang, HAN Chang-jun, LI Jing-jing, LIU Jie, ZHOU Kun, YANG Cao, WEI Qing-song. 3D printing of a titanium-tantalum gyroid scaffold with superb elastic admissible strain, bioactivity and in-situ bone regeneration capability [J]. Additive Manufacturing, 2021, 47: 102223.

[37] BRODIE E G, WEGENER T, RICHTER J, MEDVEDEV A, NIENDORF T, MOLOTNIKOV A. A mechanical comparison of alpha and beta phase biomedical TiTa lattice structures [J]. Materials & Design, 2021, 212: 110220.

[38] MAJCHROWICZ K, PAKIEŁA Z, BRYNK T, ROMELCZYK-BAISHYA B, PŁOCIŃSKA M, KURZYNOWSKI T, CHLEBUS E. Microstructure and mechanical properties of Ti Re alloys manufactured by selective laser melting [J]. Materials Science and Engineering A, 2019, 765: 138290.

[39] BRODIE E G, MEDVEDEV A E, FRITH J E, DARGUSCH M S, FRASER H L, MOLOTNIKOV A. Remelt processing and microstructure of selective laser melted Ti25Ta [J]. Journal of Alloys and Compounds, 2020, 820: 153082.

[40] ZHANG Xiao-hua, LIU Dao-xin. Effects of temperature, slip amplitude, contact pressure on fretting fatigue behavior of Ti811 alloys at elevated temperatures [J]. Acta Metallurgica Sinica (English Letters), 2009, 22(2): 131−137.

[41] BAYAT M, THANKI A, MOHANTY S, WITVROUW A, YANG Shou-feng, THORBORG J, TIEDJE N S, HATTEL J H. Keyhole-induced porosities in laser-based powder bed fusion (L-PBF) of Ti6Al4V: High-fidelity modelling and experimental validation [J]. Additive Manufacturing, 2019, 30: 100835.

[42] THIJS L, VERHAEGHE F, CRAEGHS T, van HUMBEECK J, KRUTH J P. A study of the microstructural evolution during selective laser melting of Ti−6Al−4V [J]. Acta Materialia, 2010, 58(9): 3303−3312.

[43] VRANCKEN B, THIJS L, KRUTH J P, VAN HUMBEECK J. Microstructure and mechanical properties of a novel β titanium metallic composite by selective laser melting [J]. Acta Materialia, 2014, 68: 150−158.

[44] ZHOU Ying-long, NIINOMI M, AKAHORI T. Effects of Ta content on Young's modulus and tensile properties of binary Ti−Ta alloys for biomedical applications [J]. Materials Science and Engineering A, 2004, 371(1): 283−290.

[45] SING S L, YEONG W Y, WIRIA F E. Selective laser melting of titanium alloy with 50 wt.% tantalum: Microstructure and mechanical properties [J]. Journal of Alloys and Compounds, 2016, 660: 461−470.

[46] ZHOU Ying-Long, NIINOMI M. Ti−25Ta alloy with the best mechanical compatibility in Ti−Ta alloys for biomedical applications [J]. Materials Science and Engineering: C, 2009, 29(3): 1061−1065.

[47] SHAO Yang, ZHU Wen-di, GE Li-bo, CUI Li-ying, YU Wei-kang, MA Huan. Microstructure, mechanical properties and shape memory effect of a new metastable Ti−W alloy [J]. Materials Science and Engineering A, 2024, 895: 146208.

能量密度对激光粉末床熔化 Ta–33Ti 合金显微组织与力学性能的影响

张家琪[1]，陈 超[1]，李 丹[1]，耿赵文[1]，潘 鹏[1]，王国华[2]，周科朝[1]，刘渐陵[1]

1. 中南大学 粉末冶金国家重点实验室，长沙 410083；
2. 湖南华翔医疗科技有限公司，宁乡 410600

摘 要：研究激光工艺参数对激光粉末床熔化(LPBF)制备的 Ta−33%Ti(质量分数)合金的致密化、相组成、显微组织和力学性能的影响。结果表明，在合适的能量输入下，LPBF 可以获得完全致密均匀的 Ta−Ti 零件。由于成分过冷，形成细胞状和树枝状结构。透射电子显微镜(TEM)分析表明，由于凝固前沿元素的微观偏析，细胞状结构中的层状 α'' 相倾向于集中在细胞状结构的边界。在能量密度为 166.7 J/mm^3 的条件下制备的样品具有良好的极限抗拉强度 806 MPa 和优异的杨氏模量 36.7 GPa。

关键词：Ta−Ti 合金；激光粉末床熔化；细胞状和树枝状结构；成分过冷

(Edited by Xiang-qun LI)